Research Article Vol. 38, No. 2 / February 2021 / Journal of the Optical Society of America A 245

Journal of the Optical Society of America A

OPTICS, IMAGE SCIENCE, AND VISION

Variability in atlas registration of optical intrinsic signal imaging and its effect on functional connectivity analysis

Jonah A. Padawer-Curry,[1] Jharna Jahnavi,[1] Jake S. Breimann,[1] Daniel J. Licht,[1] Arjun G. Yodh,[2] Akiva S. Cohen,[3] and Brian R. White[1,*]

[1]Department of Pediatrics, The Children's Hospital of Philadelphia, 3501 Civic Center Blvd., Room 1300.24, Philadelphia, Pennsylvania 19104, USA
[2]Department of Physics and Astronomy, University of Pennsylvania, 3231 Walnut St., Philadelphia, Pennsylvania 19104, USA
[3]Department of Anesthesiology and Critical Care Medicine, The Children's Hospital of Philadelphia, 3615 Civic Center Blvd., Abramson Research Center, Room 816-H, Philadelphia, Pennsylvania 19104, USA
*Corresponding author: whiteb1@email.chop.edu

Received 17 September 2020; revised 22 December 2020; accepted 22 December 2020; posted 6 January 2021 (Doc. ID 410447); published 22 January 2021

To compare neuroimaging data between subjects, images from individual sessions need to be aligned to a common reference or "atlas." Atlas registration of optical intrinsic signal imaging of mice, for example, is commonly performed using affine transforms with parameters determined by manual selection of canonical skull landmarks. Errors introduced by such procedures have not previously been investigated. We quantify the variability that arises from this process and consequent errors from misalignment that affect interpretation of functional neuroimaging data. We propose an improved method, using separately acquired high-resolution images and demonstrate improvements in variability and alignment using this method.

https://doi.org/10.1364/JOSAA.410447

1. INTRODUCTION

Functional neuroimaging encompasses methodologies that map brain function and functional networks to different cortical locations. Acquisition of such data necessarily occurs relative to the coordinate system of the scanner. Subject positioning varies, however, and one cannot compare raw data across subjects and scans. Therefore, to combine data, images from individual runs must be aligned to a common reference, termed an "atlas" space [1,2]. Reference atlases have been developed for humans [3–6], mice [7–10], and macaques [11]. Alignment to the atlas is often accomplished via identification of easily visualized anatomic landmarks, such as the major sulci and gyri that are visible with magnetic resonance imaging (MRI) in humans and other primates [6,12]. Variation in the identification of landmarks can arise, however, and will generally lead to errors in alignment and distortion of data comparisons [1,5,13,14]. Our goal is to understand the variation in atlas registration of optical intrinsic signal (OIS) imaging in mice and to develop methods to reduce errors and misalignment.

OIS uses visible light to measure hemodynamics within the surface of the cortex [15–18]. This approach maps neuronal physiology through neurovascular coupling, an approach similar to functional MRI (fMRI). OIS data in mice is commonly aligned to the Paxinos [7] or the Allen [8] atlases. Alignment to an atlas places the functional neuroimaging data in context with anatomic, histologic, and molecular information. In practice, atlas registration in OIS is performed by manual selection of landmarks on the skull to define an affine transformation between the acquisition (scanner) and the atlas coordinate systems [19–21]. We hypothesize that manual methods are prone to intra- and interobserver variability, bias, and errors due to differences in user expertise. Furthermore, we expect that differences in landmark selections will cause identical cortical locations to be misaligned, creating inaccuracies and lowering statistical power during subsequent stages of analysis.

In this contribution, we rigorously analyze the errors that arise from variability in landmark selection for atlas registration in OIS. Our goal is to quantify how errors propagate through the data processing stream, with the ultimate goal of assessing the resulting differences in resting-state functional connectivity analysis. As a result of these studies, and to improve the fidelity of landmark selection, we propose the use of a high-resolution "scout" image acquired separately from the functional imaging data. We anticipate this technique will offer a more user-friendly process and will improve the reliability of landmark selection in mouse OIS imaging studies.

2. METHODS

A. OIS Imaging

Mouse neuroimaging was performed using an OIS system [Fig. 1(A)] similar to that previously described [20]. Illumination was provided by four visible-light emitting diodes (M625L3-C1, M590L3-C1, M530L3-C1, and M470L3-C1, Thorlabs, Newton, NJ). Images of the cortical surface were obtained with a cooled CCD camera (Andor iXon 897, Oxford Instruments, Hawthorn, NY). Crossed polarizers eliminated specular reflection. To perform imaging, naïve *C57bl/6* mice were anesthetized with a cocktail of 10.0 mg/g Ketamine and 1.0 mg/g of Xylazine administered intraperitoneally. The scalp was reflected to expose the skull, and either an intact-skull cranial window [22] or a layer of mineral oil was placed to allow imaging. Mice were held in place with standard ear bars.

The field of view consisted of the dorsal surface of the mouse brain [Fig. 1(B)]. An imaging session consisted of up to six 5-min runs. For the present analysis, data from multiple runs in the same mouse were not concatenated or averaged; each run was analyzed independently. Images were acquired at 120 Hz sequentially in each of the four wavelengths (470, 530, 590, and 625 nm) for an overall frame rate of 30 Hz. While the native camera sensor was 512-by-512 pixels, to acquire data at this frame rate, 4-by-4 pixel binning was performed in the camera hardware, resulting in images of 128-by-128 pixels. This frame rate was chosen to prevent artifacts secondary to aliasing of systemic physiology (e.g., pulse and respiration) into the low-frequency regime where resting-state functional connectivity is performed. With anesthesia and head fixation, motion artifacts were minimal, and correction of intrascan motion was not performed. Similarly, no frames were censored due to motion artifacts.

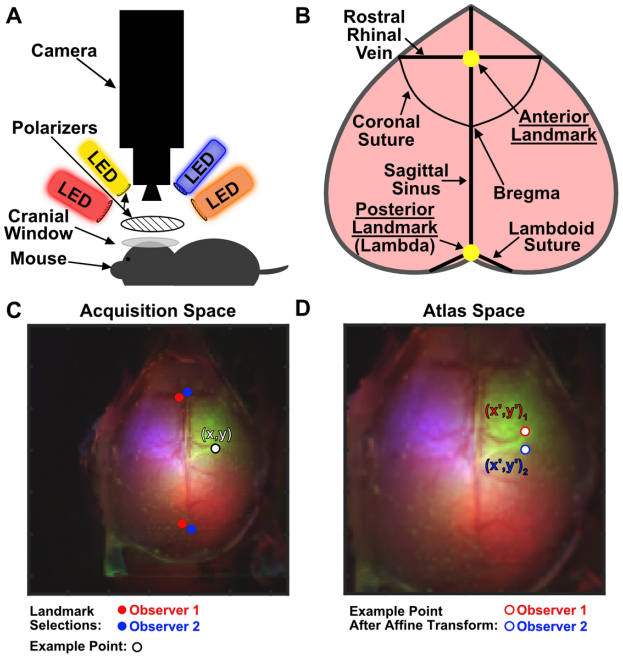

Fig. 1. Data collection and atlas registration. (A) Schematic of the imaging system demonstrating LED illumination and the camera viewing the dorsal surface of the mouse brain; (B) field of view of the imaging system. The mouse brain is viewed from above: the brain through the cranial window and skull is shown in light pink. Landmarks visible on the skull are shown in black, with locations used for atlas registration shown as yellow dots; (C) example false-color image constructed using a single functional imaging frame in order to define landmarks for atlas registration. These are the original, untransformed camera images (i.e., the scanner coordinate system). The skull and brain are visible in the center surrounded by dark hair. The landmarks, as in (B), are shown as chosen by both observers; note the variation in landmark selection. An example point (x, y) on the cortical surface is shown in white; (D) same image from (C) now shown in atlas space after atlas transformation. The example point (x, y) has been transformed using the two observers' affine transforms to two distinct locations (x', y'), resulting in misalignment.

B. Landmark Selection

To perform atlas registration, two landmarks were manually identified [Figs. 1(B) and 1(C)]: (1) an anterior landmark by the junction of the rostral rhinal vein and the sagittal suture (x_{ant}, y_{ant}), which lies on the midline between the cerebral cortex and the olfactory bulb; and (2) the lambda (x_λ, y_λ), posteriorly. Note, all (x, y) positions are relative to the origin at the lower left-hand corner of the image. The bregma is often used as a landmark for localization in stereotactic surgery, but it was not routinely visible on the OIS images and therefore was not used for atlas registration.

We compared two methods for selection of these landmarks. First, using prior standard methods [19–21], the first frame of the functional data was viewed. An observer then clicked on this 128-by-128 pixel, "binned" image to select the two desired landmarks. Second, inspired by the MRI technique of using an anatomic scan to provide registration for subsequent functional imaging, we hypothesized that using a high-resolution image for landmark selection would improve intra- and interrater reliability. Thus, prior to any functional scans, we acquired a full-resolution image from the camera (512-by-512 pixels), illuminated with the 590 nm LED. We chose this wavelength because our experience indicated that skull landmarks were easiest to visualize with this LED. We term this image the "scout" or "unbinned" image. Using this image, the same anatomic landmarks were selected, $(\hat{x}_{ant}, \hat{y}_{ant})$ and $(\hat{x}_\lambda, \hat{y}_\lambda)$. Scaled versions of these landmarks, $(\frac{\hat{x}_{ant}}{4}, \frac{\hat{y}_{ant}}{4})$ and $(\frac{\hat{x}_\lambda}{4}, \frac{\hat{y}_\lambda}{4})$, were then used as the landmark locations for the functional (128-by-128) data.

The current study includes two cohorts of mice: those scanned prior to our use of a scout image ($N = 13$) and those scanned with the collection of a high-resolution image prior to functional imaging ($N = 26$). For the first subset of mice, landmark selection data were only possible from the binned image. Note, all data for this paper were reanalyzed in a randomized and blinded fashion (as described in Section 2.E). Thus, there are no statistical or other technical differences between the earlier and later scans in how landmarks were selected from the binned images.

C. Atlas Registration

The positions of the two landmark points were also defined in an "atlas space": $(x'_{ant}, y'_{ant}) = (64.5, 110)$ and $(x_\lambda', y_\lambda') = (64.5, 15)$. Transformation to these coordinates aligns and centers the images on the midline of a 128-by-128

image [Fig. 1(D)]. In the Paxinos atlas, these two points correspond to locations (0, 3.525) and (0, −3.9), respectively; here, bregma is defined as the origin. Thus, after atlas transformation, the entire 128-by-128 pixel field of view corresponds to a 1 cm-square region in the Paxinos atlas space (each pixel is approximately 0.08 mm on each side).

Using the landmarks selected for an individual scan, an affine transform was constructed to transform the locations in "scanner space" to the target atlas space. It is important to note that, in this work, a single affine transformation will be computed for each run and applied to all frames in the functional data. Our focus is, thus, on aligning differences that arise from variation in positioning of the mouse below the camera and accounting for head shape and size. We will not be considering alignment that may be required due to motion within a scan. While motion artifacts are a major concern for fMRI, in our data, where mice are anesthetized and held in a fixed position, we have found motion artifacts to be minimal. The role of motion artifact correction in OIS, especially in awake-mouse imaging, is outside the scope of this work.

The atlas transformation consisted of rotation, translation, and a single-scale parameter (the anterior-posterior scaling was also applied to the left-right dimension). No shear component was included.

Specifically, the following terms were defined:

$$x_{\text{mid}} = \frac{x_{\text{ant}} + x_\lambda}{2}, \quad y_{\text{mid}} = \frac{y_{\text{ant}} + y_\lambda}{2},$$

$$x'_{\text{mid}} = \frac{x'_{\text{ant}} + x'_\lambda}{2}, \quad y'_{\text{mid}} = \frac{y'_{\text{ant}} + y'_\lambda}{2}, \tag{1}$$

$$s = \frac{||\,(x_{\text{ant}}, y_{\text{ant}}) - (x_\lambda, y_\lambda)\,||}{||\,(x'_{\text{ant}}, y'_{\text{ant}}) - (x'_\lambda, y'_\lambda)\,||}, \text{ and} \tag{2}$$

$$\theta = \text{atan2}\,(y_{\text{ant}} - y_\lambda, x_{\text{ant}} - x_\lambda)\,, \tag{3}$$

where *atan2* is the four-quadrant arctangent function. The affine transform can be described as a 3×3 matrix, which operates on an "augmented vector":

$$\begin{bmatrix} x' \\ y' \\ 1 \end{bmatrix} = A \begin{bmatrix} x \\ y \\ 1 \end{bmatrix}. \tag{4}$$

The affine transformation, A, consists of four component matrices:

$$A = T_2 S \Theta T_1, \tag{5}$$

where T_1 and T_2 are translation operator matrices:

$$T_1 = \begin{bmatrix} 1 & 0 & -x_{\text{mid}} \\ 0 & 1 & -y_{\text{mid}} \\ 0 & 0 & 1 \end{bmatrix}, \tag{6}$$

$$T_2 = \begin{bmatrix} 1 & 0 & x'_{\text{mid}} \\ 0 & 1 & y'_{\text{mid}} \\ 0 & 0 & 1 \end{bmatrix}. \tag{7}$$

Θ is a rotation operator matrix,

$$\Theta = \begin{bmatrix} \cos(\theta) & -\sin(\theta) & 0 \\ \sin(\theta) & \cos(\theta) & 0 \\ 0 & 0 & 1 \end{bmatrix}. \tag{8}$$

S is a scaling operator matrix,

$$S = \begin{bmatrix} s & 0 & 0 \\ 0 & s & 0 \\ 0 & 0 & 1 \end{bmatrix}. \tag{9}$$

D. Functional Connectivity

Functional data were processed as previously described [19,20], including pixel masking, high-pass and low-pass filtering (to a final frequency range of 0.009–0.8 Hz), spatial smoothing, spectroscopy, and global signal regression. These steps were repeated using affine transformations generated by both observers, A_1 and A_2. Since prior work has found no substantial differences in functional networks across hemoglobin species [19,23], and since changes in total hemoglobin ($\Delta[\text{Hb}_T]$) have been shown to have the highest signal-to-noise [23,24], all functional data we show will use $\Delta[\text{Hb}_T]$.

Functional connectivity matrices, R_1 and R_2, were then calculated for every pixel in the atlas space with a seed-based approach (i.e., each seed was a single pixel). Correlation coefficients were converted to z-scores as

$$Z = \frac{\text{atanh}(R)}{\sqrt{N-3}}, \tag{10}$$

where N is the number of points in the time series. We note that this "naïve" variance correction of $\sqrt{N-3}$ fails to account for autocorrelation in the data. However, development of a proper correction for autocorrelation in OIS is outside the scope of the present work; since the z-score values will not be used to construct p-values, the exact magnitude of the correction is not important.

E. Statistics

For all scans, landmarks were selected twice by two observers (JAPC as observer 1 and BRW as observer 2). Scans were presented to each reviewer in a random order, and observers were blinded to prior landmark selections. Variability in landmark selection (for both binned and unbinned images) was quantified using intraclass correlation coefficients (ICCs) for each of the variables x_{ant}, y_{ant}, x_λ, and y_λ.

For each landmark, and for both binned and unbinned images, differences between observer 1's and observer 2's coordinates, as well as intraobserver differences, were calculated: Δx_{ant}, Δy_{ant}, Δx_λ, and Δy_λ. For this calculation, results are displayed in units of pixels in scanner space; differences from the unbinned images were divided by 4, so that all the comparisons had equivalent units (those of the pixels in the 128-by-128 functional data). Absolute differences in pixels were also calculated as $\Delta r_i = \sqrt{\Delta x_i^2 + \Delta y_i^2}$, where i is *ant* or λ.

Next, to assess how variation in landmark selection affected alignment of cortical locations, both observers' landmark selections were used to generate affine transformations, A_1 and

A_2. While the misalignment error could be naïvely defined as $m(x, y) = ||A_1(x, y) - A_2(x, y)||$, the resulting map of error is still in the original scanner coordinate system and thus cannot be combined across mice. Rather, we define the misalignment error as the difference between these two transformations in atlas space,

$$m\left(x', y'\right) = ||\left(x', y'\right) - A_2 A_1^{-1}\left(x', y'\right)||. \quad (11)$$

This error now has units of pixels in atlas space. Values of m for all pixels in the field of view were calculated for each run, averaged across runs in a session, and then finally averaged across mice. This calculation was performed for landmarks selected for both binned and unbinned images. Canonical locations of major functional areas were selected from the Paxinos atlas [7], and the distributions of m for those locations were calculated.

We then evaluated the effect of misalignment on resting-state functional connectivity data. Functional connectivity maps were constructed using data processed with both observers' affine transforms. Example seed locations were selected based on known canonical network locations, and correlation coefficients were displayed. The difference between the two functional connectivity maps was calculated as the difference between the two z-score maps, $\Delta Z(x, y)$. The overall difference between the two maps was determined by calculating the median of the absolute value of the difference of the z-score maps: median($|\Delta Z|$). We calculated this value for all possible seed locations (i.e., every pixel), and then displayed the results as an image. These analyses were repeated for the landmarks selected from the 128-by-128 image and from the 512-by-512 image.

3. RESULTS

Data from a total of 39 mice were examined (149 total runs); for the final 23 mice, high-resolution scout images were obtained. For each scan, registration landmarks were selected twice by both observers. Agreements in landmark position were good (ICC > 0.75) for both intra- and interobserver comparisons and for both x and y coordinates (Table 1). Median absolute error was about one to two pixels in both directions (Table 1). There was worse agreement for selection of the lambda compared to the anterior landmark. Selection of landmarks from the scout image resulted in smaller errors; ICCs were higher (better agreement) and pixel errors were smaller (Table 1). Intraobserver pixel errors were smaller for observer 2 than for observer 1 ($p < 0.001$), consistent with a benefit gained from increased experience.

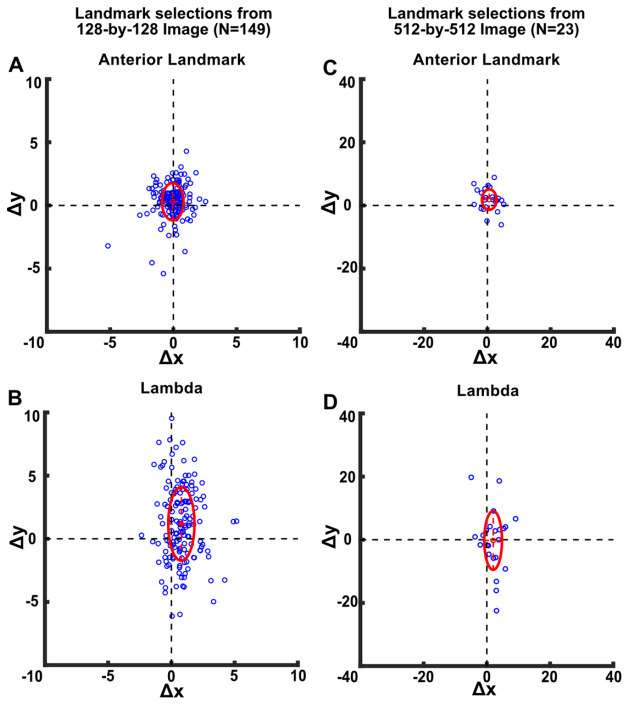

Fig. 2. Scatterplots of the differences in interobserver landmark coordinates. Units for all subfigures are pixels in scanner space. The axes have been scaled to account for differences in pixel size between the binned and scout images. (A) and (B) Variation with the binned 128-by-128 image for both the anterior landmark (A) and lambda (B); each scan is shown as a blue dot. The mean differences are shown with the red dots and standard deviations are shown as dotted lines in both the x and y directions, with an oval to clearly delineate the bounds. Absolute errors are larger for lambda than the anterior landmark. (C) and (D) Variation in landmark selection from the 512-by-512 images. Note there are fewer outliers and better agreement overall.

To visualize differences in perception of the landmark position, the distributions of differences in coordinates, Δx_i and Δy_i (for both $i = ant$ and $i = \lambda$), were plotted [Figs. 2(A) and 2(B)]. While for most runs, errors cluster around the origin (i.e., good agreement between observers), some clear outliers were apparent. Also, selection of the lambda landmark in the y (i.e., anterior-posterior) dimension resulted in fairly large errors [Fig. 2(B)]. Selection of landmarks from the scout images produced better agreement with fewer outliers [Figs. 2(C) and 2(D)]. In particular, the lambda was more easily visible with the scout images.

Table 1. Intra- and Interobserver Agreement for Landmark Selection[a,b]

128-by-128 Image	Intra 1	Intra 2	Intra 3	512-by-512 Image	Intra 1	Intra 2	Intra 3
ICC: X_{ant}/Y_{ant}	0.985/0.959	0.985/0.973	0.984/0.948	ICC: X_{ant}/Y_{ant}	0.992/0.989	0.997/0.993	0.994/0.983
ICC: X_λ/Y_λ	0.982/0.844	0.985/0.888	0.971/0.767	ICC: X_λ/Y_λ	0.985/0.848	0.996/0.939	0.990/0.847
r_{ant} (pixels)	1.18 [0.70, 1.90]	0.97 [0.60, 1.35]	1.08 [0.71, 1.86]	r_{ant} (pixels/4)	0.83 [0.54, 1.35]	0.68 [0.37,1.00]	1.05 [0.67, 1.40]
r_λ (pixels)	2.01 [1.18, 3.33]	1.74 [1.01,2.46]	2.59 [1.49, 4.04]	r_λ (pixels/4)	1.87 [1.06, 3.11]	1.25 [0.46, 1.98]	1.55 [0.94, 2.78]

[a]For both 128-by-128 and 512-by-512 images, ICCs are presented as x/y pairs (ICCs range from 0 to 1, with 1 being perfect agreement).

[b]The absolute differences in landmark selections (r) are shown as median and intraquartile ranges with units of pixels (in scanner space). For the 512-by-512 image, the pixel distances are divided by 4 to account for differences in pixel size caused by binning.

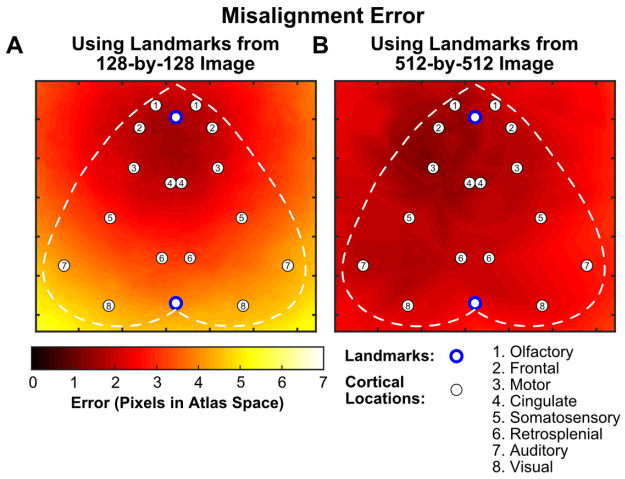

Fig. 3. Maps of misalignment at each pixel location due to differences between the two observers' landmark selections. Both images are shown in atlas space (total field of view: 128-by-128 pixels; units are pixels in the atlas space). The landmarks are shown in blue. Bilateral canonical cortical locations from the Paxinos atlas are shown in white. A typical outline of the exposed cortical surface is shown with the dashed white line. (A) Misalignment error induced by differences between the two affine transformations defined by landmark selection from the binned, 128-by-128 image. Errors are larger towards the lambda and toward the periphery. (B) Misalignment error between the two affine transformations defined by landmark selection from the unbinned, 512-by-512 scout image. Errors are substantially smaller with the landmarks selected from the high-resolution scout image.

We then examined how these errors affect alignment across the field of view of the mouse brain. Averaged misalignment errors were larger near the lambda landmark than near the anterior landmark [Fig. 3(A)], consistent with the distributions seen in Fig. 2. Additionally, errors were larger around the periphery of the field of view [Fig. 3(A)], because even small errors in scale or angle cause larger errors farther from the midpoint of the two landmarks. Thus, functional areas posteriorly and laterally (e.g., visual cortex and retrosplenial cortex) were most affected by misalignment (Table 2).

Misalignment was dramatically improved by using the affine transformations generated by the scout (unbinned) imaging [Fig. 3(B)]. In particular, posterior and lateral cortical areas had improvements in misalignment by more than a factor of 2 (Table 2). Additionally, there was no longer a bias where anterior locations had better alignment than posterior locations.

In turn, differences in landmark selection resulted in misalignment of functional connectivity matrices (Fig. 4). Functional connectivity relies on calculating correlation coefficients between the time course at a selected cortical location (the seed) and other cortical locations. The goal of atlas registration is that a given coordinate in atlas space corresponds to a particular cortical location, and differences in correlation networks across subjects or times are due to differences in the underlying neural anatomy or physiology. However, due to different alignments to the atlas by different observers, the same seed (i.e., the same pixel) in atlas space will correspond to different anatomic locations with possibly large consequences.

This issue is apparent in Fig. 4; notice that the same pixel could appear to be part of either the visual [Fig. 4(C)] or retrosplenial [Fig. 4(D)] network, depending on which atlas transformation was used. To quantify these errors, overall misalignment of functional connectivity maps was calculated by differences in z-scores. Using landmark selection from the 128-by-128 images, error could be substantial across the field of view [Fig. 4(E)]. Seed pixels at the periphery or near the midline were most vulnerable to functional connectivity correlation errors due to misalignment [Fig. 4(F)]. Using landmarks selected from the scout image, all of these errors were substantially reduced [Figs. 4(G) and 4(L)].

4. DISCUSSION

We performed the first systematic examination of errors that arise during atlas registration in OIS imaging of mice. While agreement within and between observers was often excellent when quantified by ICCs, small differences in landmark selection resulted in significant misalignment across the entire field of view after atlas transformation. The horizontal (x) direction generally had smaller errors, likely as the midline is easier to identify due to symmetry. The position of the lambda in an

Table 2. Misalignment Error (Units of Pixels in Atlas Space) at Canonical Cortical Locations (Reported as Median and Interquartile Range, IQR) due to Differences between the Two Observers' Landmark Selections[a]

	Interobserver Misalignment (Pixels in Atlas Space) Median [IQR]			
	Landmark Selection 128-by-128 Image $N = 149$		Landmark Selection 512-by-512 Image $N = 23$	
	Left	Right	Left	Right
Olfactory	1.9 [1.2, 3.1]	1.9 [1.2, 3.0]	2.0 [1.2, 2.4]	1.6 [1.0, 2.3]
Frontal	1.9 [1.2, 3.1]	1.8 [1.2, 2.8]	1.9 [1.1, 2.8]	1.4 [0.8, 2.3]
Cingulate	1.9 [1.1, 3.0]	1.9 [1.1, 2.9]	1.5 [1.0, 2.3]	1.5 [1.0, 2.3]
Motor	2.2 [1.3, 3.2]	2.0 [1.4, 2.9]	1.8 [1.2, 2.7]	1.3 [1.0, 2.3]
Somatosensory	3.1 [1.7, 4.6]	2.9 [1.9, 4.1]	2.2 [1.2, 3.4]	1.9 [0.9, 2.1]
Retrosplenial	3.1 [2.0, 4.7]	3.2 [1.9, 4.6]	2.1 [1.1, 3.4]	1.9 [1.1, 3.2]
Visual	4.3 [2.7, 6.7]	4.4 [2.6, 6.5]	2.3 [1.6, 5.1]	2.2 [1.4, 4.4]
Auditory	4.3 [2.7, 6.4]	4.1 [2.6, 6.1]	2.7 [1.7, 5.0]	1.9 [1.3, 3.7]

[a]Use of the high-resolution image resulted in substantial decreases in error, especially for locations that were more lateral or posterior (i.e., somatosensory, retrosplenial, visual, and auditory).

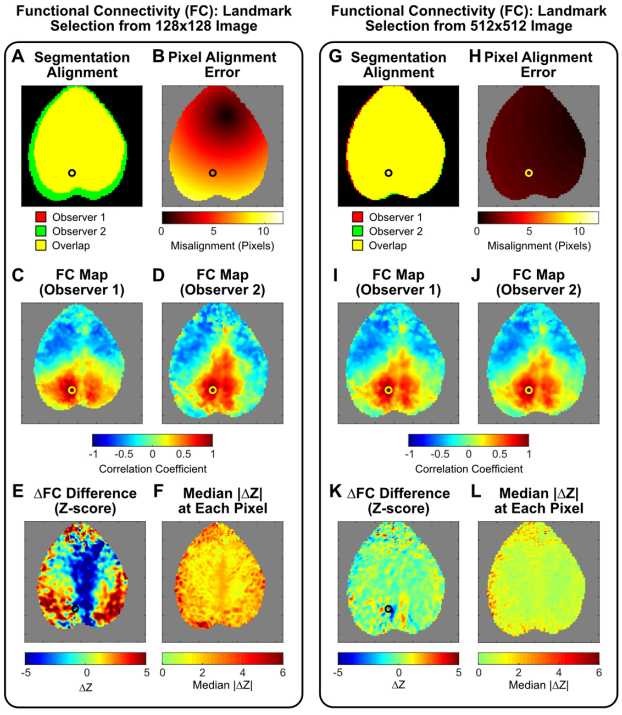

Fig. 4. Effects of variation and misalignment from different atlas transformations on functional connectivity (FC) analysis as demonstrated by an exemplar data set. (A) Variation in the alignment of the brain segmentation after both observers' affine transformations. Note that landmark selection differences have resulted in different scale factors and misalignment posteriorly. (B) Misalignment error (as in Fig. 3 with units of pixels in atlas space) demonstrating that errors are greater posteriorly and laterally. (C) and (D) Seed-based FC correlation maps based on each observer's atlas transformations. Note that for observer 2 (D), this pixel is within the retrosplenial cortex, but for observer 1 (C), this pixel is on the border of the retrosplenial and visual networks, demonstrating how misalignment can result in differences in interpretation of functional architecture. (E) Differences in the two FC maps, (C) and (D), expressed as the difference in z-scores. Large differences are present across the cortex. (F) Median differences in z-score for all possible seed pixels in the field of view. Differences are most pronounced at the periphery where misalignment errors are greatest, and along the midline, where misalignment could result in placement in the incorrect hemisphere. (G)–(L) Similar analysis using landmarks selected from the 512-by-512 scout image. Alignment of the brain segmentations is much improved (G), with resulting lower pixel misalignment errors (H). The two FC maps, (I) and (J), are very similar, showing the retrosplenial network. This similarity is quantified by the lower differences in z-scores for this seed location (K) as well as for all pixels (L).

anterior-posterior direction was particularly prone to variation in identification, as the lambdoid sutures in this area were difficult to identify, especially in the binned images.

These misalignment errors had major effects on functional connectivity analysis. Functional regions could be poorly aligned to the atlas, resulting in large errors in correlation coefficients. Furthermore, these effects were not spatially consistent. Errors were larger at the periphery (as even small errors in rotational alignment are magnified further from the center of the image). With the binned images, errors were larger near the lambda. When conducting statistical tests of functional connectivity across subjects, this positional bias in the data's variance could induce spurious results when not properly accounted for.

We developed a novel method to ameliorate these issues. The key was to use a high-resolution scout image acquired prior to functional data acquisition to improve the ease of landmark selection. Using these images, we showed that we were able to more clearly resolve landmarks, lowering intra- and interobserver variability of landmark selection. As a result of decreased variability in landmark selection, misalignment error was lowered across the entire field of view after atlas transformation. This improvement, in turn, produced better alignment of functional connectivity maps and better agreement in correlation coefficients.

Advanced methods for atlas registration have been developed for fMRI (where high spatial resolution and cortical folding necessitate accuracy) [6,12,14] and diffuse optical tomography (DOT, where probe positioning can be highly variable from run to run or subject to subject) [25,26]. To our knowledge, such methods have not been explored for OIS imaging, perhaps because the mouse brain has minimal folding and the functional neuronal architecture is simpler. Thus, localization errors for OIS would seem to be less of a concern. However, we have shown that even small differences in the landmarks that define the affine transformation can result in large downstream errors. Our use of a high-resolution scout image is a first step toward improving ease of use and decreasing errors that were previously overlooked. The importance of accurate atlas registration for rigorous human neuroimaging based on near-infrared spectroscopy (NIRS) or DOT has been increasingly recognized [25–29]. Our results demonstrate that similar attention should be paid to these analytical steps in mouse neuroimaging. By reducing variation that arises due to experimental technique, the remaining variation can be more reliably attributed to true differences in anatomy and physiology. Reduced experimental "noise" will also improve the statistical power of neuroimaging studies.

Our acquisition of an initial, high-resolution image of the mouse brain was inspired by ideas from fMRI, where functional data is aligned using dedicated, anatomic MRI obtained within the same imaging session [5]. In the future, we will explore additional methods to improve the atlas registration process. First, the use of more than two landmarks should improve accuracy, since the affine transformation variables would be overdetermined; error in any individual landmark would then have a smaller effect on the final alignment. Other skull landmarks (e.g., the bregma), which were difficult to clearly visualize in the functional data, may be more readily visible in high-resolution images, thereby facilitating improved alignment. Ideally, a lateral landmark would enable separate calculation of horizontal and vertical scaling factors. Unfortunately, no major landmarks fall within our field of view except those on the midline. Perhaps in the future, the use of computer vision algorithms might offer the ability to use distributed landmarks not obvious to the human eye. Additionally, the development of such automated or semiautomated techniques, similar to those commonly used for fMRI, would rely less on observer expertise, which would further increase ease of use and increase statistical rigor.

One limitation of our work was that we considered only resting-state functional connectivity data sets using single pixel seeds. The error due to misalignment will clearly depend on the magnitude of the misalignment compared to the size of the functional region and seed. Here, we elected to use single pixels as our seeds so that all scans (each with a different spatially distributed error) would be on an equal footing. In practice, the use of seeds with larger spatial extent would blur (and thus mitigate) the effects of small errors in alignment. Conversely, misalignment errors may be more significant for task- or stimulus-based paradigms. The precise cortical regions that can be localized with tasks are of the same size as the misalignment errors demonstrated in our work. Misalignment could, thus, result in artificially blurred activations when averaged across subjects.

With any camera there are trade-offs between temporal resolution, spatial resolution, and dynamic range. Our use of a separate high-resolution scout image was necessitated by the desire to acquire functional data at a frame rate far above systemic cardiovascular physiology and thereby avoid aliasing artifacts in the low-frequency regime. As functional neuroimaging is possible with fMRI, where the frame rate is well below either the mouse or human pulse or respiratory rate, such aliasing clearly does not prevent advanced analysis. However, the effect of aliasing in mice with OIS has not been fully explored. The use of slower frame rates (or the use of future camera technology that would allow higher-resolution imaging at high speed) could permit the acquisition of functional data without binning. Alternatively, a separate high-resolution color camera could be coupled into the optical path to enable simultaneous recording of both functional and anatomic data.

Additionally, we did not explicitly evaluate learning-curve effects. For example, the lower pixel errors for observer 2 compared to those of observer 1 suggest that landmark selection accuracy improves with experience. Use of a standardized instructional method to teach landmark selection may improve performance. Ultimately, use of OIS should become more universally applicable if methods could be developed that are less sensitive to user error and experience.

5. CONCLUSIONS

In summary, we have quantified error in landmark selection, and we have quantified how this error affects the analysis of resting-state functional connectivity data. Although such errors may appear to be less important than other aspects of data analysis, accurate alignment of functional data is a key parameter for statistical analysis of large data sets. Improving the atlas registration process should improve the rigor and reliability of preclinical imaging with OIS. Our method of using a high-resolution image prior to functional data acquisition is an easily implemented method to improve the accuracy of alignment and thus improve the data quality of optical neuroimaging in mice.

Funding. National Institute of Neurological Disorders and Stroke (K08-NS117897, R01-NS060653); Eunice Kennedy Shriver National Institute of Child Health and Human Development (R37-HD059288); National Institute of Biomedical Imaging and Bioengineering (P41-EB015893); National Heart, Lung, and Blood Institute (T32-HL007915); Children's Hospital of Philadelphia.

Disclosures. The authors declare no conflicts of interest.

REFERENCES

1. M. Brett, I. S. Johnsrude, and A. M. Owen, "The problem of functional localization in the human brain," Nat. Rev. Neurosci. **3**, 243–249 (2002).
2. M. V. Wyawahare, P. M. Patil, and H. K. Abhyankar, "Image registration techniques: an overview," Int. J. Signal Process. Image Process. Pattern Recogn. **2**, 11–28 (2009).
3. J. L. Lancaster, M. G. Woldorff, L. M. Parsons, M. Liotti, C. S. Freitas, L. Rainey, P. V. Kochunov, D. Nickerson, S. A. Mikiten, and P. T. Fox, "Automated Talairach atlas labels for functional brain mapping," Hum. Brain Mapp. **10**, 120–131 (2000).
4. P. K. Mandal, R. Mahajan, and I. D. Dinov, "Structural brain atlases: design, rationale, and applications in normal and pathological cohorts," J. Alzheimer's Dis. **31**, S169–S188 (2012).
5. A. C. Evans, A. L. Janke, D. L. Collins, and S. Baillet, "Brain templates and atlases," NeuroImage **62**, 911–922 (2012).
6. D. C. van Essen, "Cortical cartography and caret software," NeuroImage **62**, 757–764 (2012).
7. G. Paxinos and K. B. J. Franklin, *Paxinos and Franklin's the Mouse Brain in Stereotaxic Coordinates* (Academic, 2019).
8. H. W. Dong, *The Allen Reference Atlas: A Digital Color Brain Atlas of the C57Bl/6J Male Mouse* (Wiley, 2008).
9. A. MacKenzie-Graham, E.-F. Lee, I. D. Dinov, M. Bota, D. W. Shattuck, S. Ruffins, H. Yuan, F. Konstantinidis, A. Pitiot, Y. Ding, G. Hu, R. E. Jacobs, and A. W. Toga, "A multimodal, multidimensional atlas of the C57BL/6J mouse brain," J. Anat. **204**, 93–102 (2004).
10. G. A. Johnson, A. Badea, J. Brandenburg, G. Cofer, B. Fubara, S. Liu, and J. Nissanov, "Waxholm space: an image-based reference for coordinating mouse brain research," Neuroimage **53**, 365–372 (2010).
11. S. Frey, D. N. Pandya, M. M. Chakravarty, L. Bailey, M. Petrides, and D. L. Collins, "An MRI based average macaque monkey stereotaxic atlas and space (MNI monkey space)," Neuroimage **55**, 1435–1442 (2011).
12. D. C. van Essen, "Surface-based approaches to spatial localization and registration in primate cerebral cortex," NeuroImage **23**, S97–S107 (2004).
13. A. Sarkar, R. J. Santiago, R. Smith, and A. Kassaee, "Comparison of manual vs automated multimodality (CT-MRI) image registration for brain tumors," Med. Dosim. **30**, 20–24 (2005).
14. M. Wu, O. Carmichael, P. Lopez-Garcia, C. S. Carter, and H. J. Aizenstein, "Quantitative comparison of AIR, SPM, and the fully deformable model for atlas-based segmentation of functional a structural MR images," Hum. Brain Mapp. **27**, 747–754 (2006).
15. A. Grinvald, E. Lieke, R. D. Frostig, C. D. Gilbert, and T. N. Wiesel, "Functional architecture of the cortex revealed by optical imaging of intrinsic signals," Nature **324**, 361–364 (1986).
16. D. Y. Ts'o, R. D. Frostig, E. E. Lieke, and A. Grinvald, "Functional organization of primate visual cortex revealed by high resolution optical imaging," Science **249**, 417–420 (1990).
17. T. A. Woolsey, C. M. Rovainen, S. B. Cox, M. H. Henegar, G. E. Liang, D. Liu, Y. E. Moskalenko, J. Sui, and L. Wei, "Neuronal units linked to microvascular modules in cerebral cortex: response elements for imaging the brain," Cereb. Cortex **6**, 647–660 (1996).
18. A. K. Dunn, A. Devor, A. M. Dale, and D. A. Boas, "Spatial extent of oxygen metabolism and hemodynamic changes during functional activation of the rat somatosensory cortex," NeuroImage **27**, 279–290 (2005).
19. B. R. White, A. Q. Bauer, A. Z. Snyder, B. L. Schlaggar, J.-M. Lee, and J. P. Culver, "Imaging of functional connectivity in the mouse brain," PLoS One **6**, e16322 (2011).
20. B. R. White, J. A. Padawer-Curry, A. S. Cohen, D. J. Licht, and A. G. Yodh, "Brain segmentation, spatial censoring, and averaging techniques for optical functional connectivity imaging in mice," Biomed. Opt. Express **10**, 5952–5973 (2019).
21. A. Q. Bauer, A. W. Kraft, P. W. Wright, A. Z. Sndyer, J.-M. Lee, and J. P. Culver, "Optical imaging of disrupted functional connectivity following ischemic stroke in mice," NeuroImage **99**, 388–401 (2014).

22. G. Silasi, D. Xiao, M. P. Vanni, A. C. N. Chen, and T. H. Murphy, "Intact skull chronic windows for mesoscopic wide-field imaging in awake mice," J. Neurosci. Methods **267**, 141–149 (2016).
23. S. Kura, H. Xie, B. Fu, C. Ayata, D. A. Boas, and S. Sakadžić, "Intrinsic optical signal imaging of the blood volume changes is sufficient for mapping the resting state functional connectivity in the rodent cortex," J. Neural Eng. **15**, 035003 (2018).
24. B. R. White, J. A. Padawer-Curry, T. Ko, W. Baker, J. Breimann, A. S. Cohen, D. J. Licht, and A. G. Yodh, "Wavelength censoring for spectroscopy in optical functional neuroimaging," Phys. Med. Biol. (to be published).
25. S. L. Ferradal, A. T. Eggebrecht, M. Hassanpour, A. Z. Snyder, and J. P. Culver, "Atlas-based head modeling and spatial normalization for high-density diffuse optical tomography: in vivo validation against fMRI," NeuroImage **85**, 117–126 (2014).
26. R. J. Cooper, M. Caffini, J. Dubb, Q. Fang, A. Custo, D. Tsuzuki, B. Fischl, W. Wells, III, I. Dan, and D. A. Boas, "Validating atlas-guided DOT: a comparison of diffuse optical tomography informed by atlas and subject-specific anatomies," NeuroImage **62**, 1999–2005 (2012).
27. A. Custo, D. A. Boas, D. Tsuzuki, I. Dan, R. Mesquita, B. Fischl, W. E. L. Grimson, and W. Wells, III, "Anatomical atlas-guided diffuse optical tomography of brain activation," Neuroimage **49**, 561–567 (2010).
28. D. Tsuzuki, D. Cai, H. Dan, Y. Kyotoku, A. Fujita, E. Watanabe, and I. Dan, "Stable and convenient spatial registration of stand-alone NIRS data through anchor-based probabilistic registration," Neurosci. Res. **72**, 163–171 (2012).
29. H. Santosa, X. Zhai, F. Fishburn, and T. Huppert, "The NIRS brain AnalyzIR toolbox," Algorithms **11**, 73 (2018).